C. R. Chimie 22 (2019) 648–658

Contents lists available at ScienceDirect

Comptes Rendus Chimie

www.sciencedirect.com

Full paper / Mémoire

Effects of Sr^{2+}, Fe^{3+} and Al^{3+} doping on the properties of TiO_2 prepared using the sol–gel method

Abderraouf Jraba [a, b, *], Zohra Anna [a, c], Elimame Elaloui [a, c]

[a] Laboratory of Materials, Energy and Environment UR 14/ES 26, University of Gafsa, 2100 Gafsa, Tunisia
[b] Faculty of Sciences of Gabes, Erriadh City, 6072 Zrig Gabès, Tunisia
[c] Department of Chemistry, Faculty of Sciences of Gafsa, Sidi Ahmed Zarroug, 2100 Gafsa, Tunisia

ARTICLE INFO

Article history:
Received 21 June 2019
Accepted 9 October 2019
Available online 15 November 2019

Keywords:
Doped TiO_2
Solgel
Transparent
Monolith
Metal-doped

ABSTRACT

The present study aims to synthesize highly active and transparent monoliths of Al-, Fe- and Sr-doped TiO_2. These photocatalysts were synthesized for the first time using a simple modified solgel process. Titanium isopropoxide was used as a precursor of titanium. The control of hydrolysis and polycondensation of the precursor were mediated by the esterification reaction between acetic acid and the solvent at room temperature. The doped monoliths prepared by this method were transparent at wavelengths ranging from 500 nm to 800 nm. The noncalcinated Al–TiO_2 and Fe–TiO_2 crystallized in the anatase form. Powder X-ray diffraction confirmed the amorphous-to-anatase and the anatase brookite to-rutile phase transformations at different treatment temperatures. Based on the obtained results, only the anatase form was observed in all samples calcined at 450 °C. According to the N_2 adsorption/desorption analysis, transparent gels had a larger surface area and high porosity. Al–TiO_2 showed improved photocatalytic performance in the photodegradation of methylene blue (MB) upon UV irradiation. Fe–TiO_2 exhibited a good yield for the degradation of MB upon solar irradiation. This study uses transparent monoliths as a novel approach to achieve the required findings.

1. Introduction

Porous and transparent metal oxides have attracted increasing interest because of their wide range of potential applications [1–3]. Transparent glass composed of silica is the most well-studied oxide [4–6]. Other functional porous oxides, including titania, have also attracted considerable attention [7,8]. Titanium dioxide has applications in many areas, such as photocatalysis and electrocatalysis [9], detectors [10,11], energy storage [12], medical applications [13] and solar cells [14]. It has attracted increasing attention and has a very wide range of uses, because of its excellent photonic activity, high stability, nontoxicity and low cost. TiO_2 has three different crystalline phases: anatase, rutile and brookite [15]. The anatase phase of TiO_2 is characterized by a large bandgap and high electron mobility. This phase of TiO_2 is most interesting when it is used in dye-sensitized solar cells [16] and for photodegradation [17]. TiO_2 has a very high reactivity and chemical stability upon exposure to ultraviolet (λ <400 nm) or visible light.

Titania xerogel represents one of the most promising classes of porous titania because of the unique properties inherent to these materials, namely, a high porosity and a low density. Different methods have been used to synthesize TiO_2. Among these processes, the classic sol–gel method requires less energy and less time, and the materials prepared by this method are very diverse at the nanoscale. Doping with a small quantity of different elements potentially alters the structure and electronic properties of the oxides. The doping species is substituted

* Corresponding author. Laboratory of Materials, Energy and Environment UR 14/ES 26, University of Gafsa, 2100 Gafsa, Tunisia.
E-mail address: jrabaraoof@gmail.com (A. Jraba).

https://doi.org/10.1016/j.crci.2019.10.003
1631-0748/

by atoms in the host metal oxide [18]. Several TiO_2 modifications have been proposed: doping with the transition metals Cu, Co, Ni, Fe, Ru, Au, Ag and Pt [19–23], non–metal-doped TiO_2 [24], composites of TiO_2 [25–27] and TiO_2 doped with rare-earth elements [28].

In addition, doping modifies the forbidden band, which positively modulates the process of electron-hole separation and recombination [29]. In addition, the doping process increases the number of adsorbed dyes on the surface by increasing the surface area of the semiconductor.

Several methods have been used to prepare titania wet gels and xerogel monoliths [30,31]. However, very few investigations have obtained transparent titania xerogels [32–37]. Transparent doped titania xerogels have been efficiently used as coatings for antifogging mirrors [38], solar cells and chemical or medical sensors [30].

The present study was divided into two parts. The first was devoted to analyzing the effect of synthesis parameters on the gel time of transparent Fe-, Al- and Sr-doped titanium dioxide and the evolution of transparency as function of the dopant properties. Samples that make the subject of the second part is those that present higher transparency. The second part aimed to study the effects of Fe^{3+}, Sr^{2+} and Al^{3+} doping on enhancing the physicochemical properties of selected TiO_2 and the optical properties of these photocatalysts. Physicochemical studies focused on the crystallinity, surface morphology and thermal stability of monoliths, while optical properties of doped TiO_2 were monitored using an ultraviolet-visible diffuse reflectance spectrophotometer (UV-vis DRS). Finally, the catalytic efficiency of selected doped titanium dioxide monoliths was assessed by monitoring the degradation of methylene blue (MB) upon UV and solar irradiation.

2. Experimental study

2.1. Monolith synthesis

The chemical reagents used in the present study were titanium(IV) tetraisopropoxide ($Ti(iOPr)_4$, 97%; Sigma-Aldrich), glacial acetic acid (99.8%; Panréac), anhydrous aluminium(III) chloride ($AlCl_3$, 97%; Sigma-Aldrich), anhydrous iron(III) chloride ($FeCl_3$, 97%; Sigma-Aldrich), anhydrous strontium nitrate ($SrNO_3$, >99%; Sigma-Aldrich), absolute ethanol (C_2H_6O, >99.8%; Sigma-Aldrich), absolute isopropanol (C_3H_8O, 100%; Sigma-Aldrich) and absolute 1-butanol ($C_4H_{10}O$, 99.5%; Sigma-Aldrich).

The synthesis protocol used in this study is shown in Fig. 1 of the supplementary data and was based on the study by El Mir et al. [37]. Seven millilitres of the solvent (alcohol) was mixed with 1.5 ml of glacial acetic acid while stirring. After 1 h of stirring (esterification reaction between acetic acid and alcohol), 5 ml of the precursor was added and a clear and stable solution was obtained. After 30 min of stirring the whole mixture, 0.5 ml of the salt solution was added. The molar ratio between solvent, precursor, glacial acetic acid and metallic salt was 14:10:x:y, where $x = 0$, 0.5, 1, 1.5 and 2, and $y = 0.5$, 0.75 and 1.

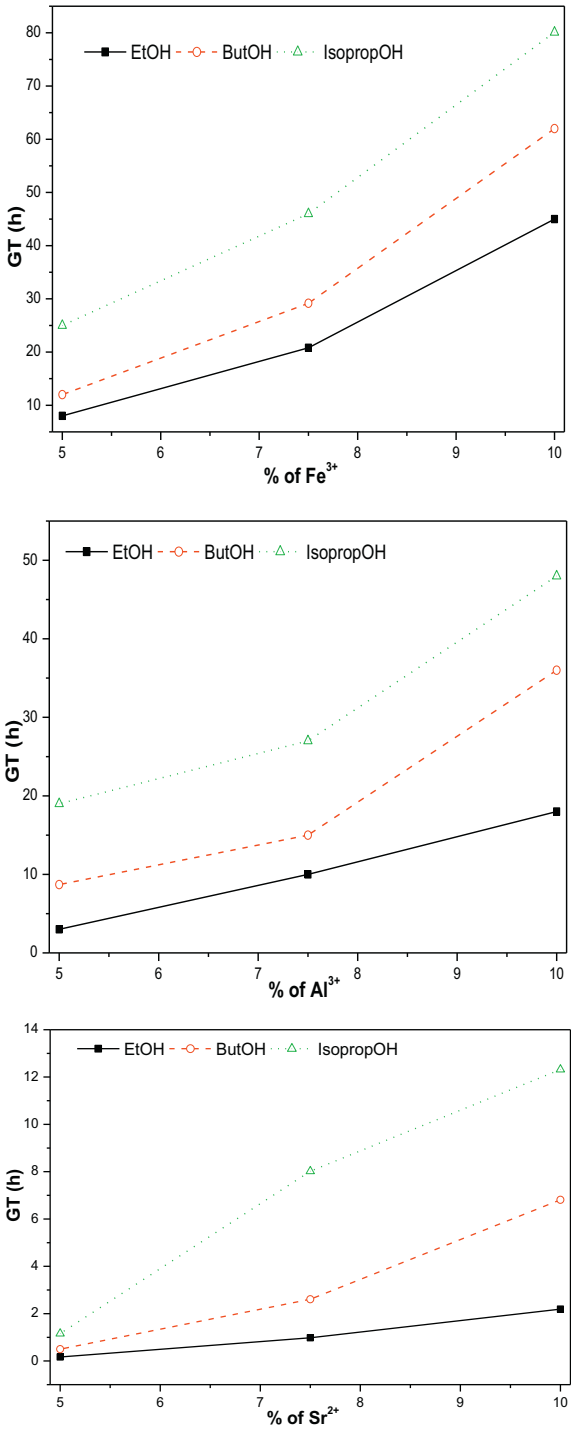

Fig. 1. Evolution of the GT according to the nature of dopant, dopant concentration and solvent (with $V_{AcA} = 1.5$ ml). GT, gel time.

2.2. Monolith characterization

The crystal structures of the samples were determined using a PANanalytical X'Pert Pro wide-angle X-ray powder diffractometer, equipped with a copper anticathode that produced Cu K_α radiation at 1.5418 Å.

Table 1
Variation in GT (h) as a function of the Ac.A molar ratio with different solvents (the dopant concentration was fixed at 10%).

Ac.A molar ratio	GT (h)								
	Ethanol			Butanol			Isopropanol		
	Fe	Sr	Al	Fe	Sr	Al	Fe	Sr	Al
0	0	0	0	0	0	0	0	0	0
0.5	23	1.5	15	43	5	18	52	11	30
1	28	1.8	16.4	51	5	27	61	9	33
1.5	45	2	18	62	6	36	80	12	48
2	70	7	38	87	17	37	102	24	64

GT, get time.

The recorded diffractogram corresponded to as-prepared samples and calcinated xerogels under air flow for 4 h at 773 K and 923 K. The Fourier-transform infrared (FTIR) spectra of all samples were obtained using a SHIMADZU 8400S instrument. The spectra of solids were obtained using KBr pellets. Before the measurements, the xerogel and KBr were mixed at a quality ratio of 1:100.

The PerkinElmer STA 6000 simultaneous thermal analyzer allowed us to record the thermogravimetric and differential thermogravimetric analysis (TGA-DTG) thermographs. The UV-vis absorption spectra were recorded with absorbance and % transmittance using a PerkinElmer LAMBDA 1050 UV/Visible/NIR spectrophotometer. The bandgap energy was calculated using a graphical method by plotting the variation in $(\alpha h\nu)^{1/n}$ versus $(h\nu)$ with the Tauc relation: $(\alpha h\nu)^{1/n} = f(h\nu)$,
where

α is the absorption coefficient,
h is the Planck constant,
ν is the wave number.

The textural characteristics were analyzed using an ASAP2020 Micrometrics physical nitrogen adsorption/desorption instrument.

Generally, the thermal analysis aimed to study changes in the behaviour of the material as a function of temperature, including dehydration, enthalpy, weight loss, fusion, decomposition, phase analysis, etc.

The TGA/DTG thermograms of gels were recorded using a PerkinElmer STA 6000 instrument. An alumina crucible was used to heat the powders. This thermal analysis was conducted under an area atmosphere (60 ml/min) with a heating rate of 10 °C/min at temperatures ranging from 32 to 900 °C. The initial weights of the analyzed materials were 17.90 mg of Al–TiO_2, 11.32 mg of Fe–TiO_2 and 11.44 mg of Sr–TiO_2.

2.3. Photocatalytic assay

We evaluated the photocatalytic behaviour of the synthesized xerogels by monitoring the degradation of MB upon UV and solar irradiation in an aqueous solution. The reactor used for the UV degradation is presented in supplementary data Fig. 2 and was the same reactor used by Kachbouri et al. [17]. It comprises two HEROLAB UV 4 SL 8 W emitting two UV wavelengths (254 and 365 nm), an aluminium cover, one 80-ml volumetric cylinder and a magnetic stirrer.

For degradation induced by sunlight, adsorption was performed in the previous assembly, and then the mixture (dye solution and catalyst) was exposed to sunlight under rigorous agitation.

One hundred milligrams of photocatalyst was suspended in 80 ml of a 30-mg/L MB solution. The suspension was stirred for 60 min in dark to ensure an even dispersion of the photocatalyst and an adsorption-desorption equilibrium. The mixture was irradiated with the two lamps at *a* wavelength of 254 nm. The progress of the reaction was followed by periodic manual sampling. The samples were filtered through a 0.45-μm membrane, and the concentration of MB was measured using a UV-visible spectrophotometer at 664 nm.

3. Results and discussion

3.1. Gel time and transparency

3.1.1. Effect of salts on the gel time

Fig. 1 presents the variation in gel time (GT) as a function of the concentration and type of metallic salts and solvents used. Note that the GT increased as the type of alcohol varied, regardless of the doping metal. This variation is potentially explained by the effect of alcohol type on the esterification reaction that generates water for hydrolysis and condensation of the titanium precursor. The changes in GT as a function of alcohol type are consistent with the results reported by Kesmez et al. [39]. On the other hand, the GT increased as a function of the percentage of the doping reagent, which is explained by two phenomena. The first phenomenon was reported by Hasegawa et al. [40], who presumed that Ti^{4+} changed its oxidation number from +IV to +VI to enable its hexacoordination with anions (Cl^- and NO_3^-). The formation of these complexes causes competition with the germination of the crystalline lattice. This competition is manifested by an increase in the GT. The second explanation was based on the difference in the acidic capacity of the dopants. $FeCl_3$ is more acidic than $AlCl_3$ [41], which is more acidic than $SrNO_3$, and a decrease in the pH of the medium favours the hydrolysis of the precursor and not polycondensation. The increase in GT as a function of the type of doping metal is consistent with the results of previous studies in this field.

3.1.2. Effect of the amount of acetic acid (Ac.A)

Table 1 shows an increase in the GT with an increase in the molar ratio of added acetic acid (catalyst) in the presence of 10% added metal. This variation was explained as followed by Parra et al. [42]: the acetate anions function as bidentate ligands and are fixed on Ti^{4+} cations in either a chelating or bridging manner (Eqs. 1 and 2). These two types of bonds inhibit the progression of polycondensation (Fig. 2) which increases the GT of the sol. The variation in the GT was more significant for samples doped with Fe^{3+} and Al^{3+}, and this difference was due to the increase of the pH of the solution generated by the Lewis acid behaviour of these dopants.

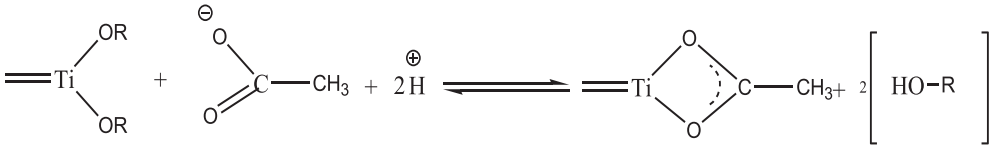

Equation 1: Bridging acetate formation reaction [42].

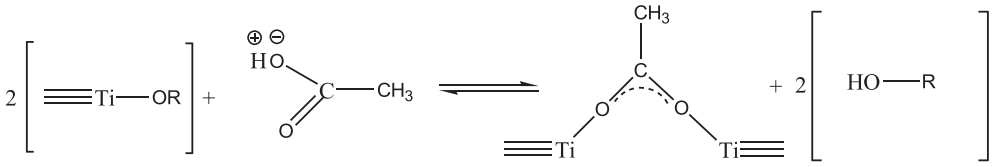

Equation 2: Formation reaction in which acetate is chelated [42].

3.1.3. Transparency of gels

The transparency of samples only depends on the metal type. Using the chosen synthetic route, better transparency was observed under the optimum conditions: ethanol as the solvent, an acetic acid molar ratio of 1.5 and 10% concentration of the dopant. These results are shown in Fig. 3. The results were discussed based only on the nature of the salt.

As shown Fig. 3, pure TiO_2 was opaque, while Fe—TiO_2 and Al—TiO_2 were more transparent than Sr—TiO_2. The opacity of undoped TiO_2 confirmed that acetate anions did not effect the transparency of the samples. This result contradicts the findings reported by Elghniji et al. [36]. Acetate reacts with Ti^{4+} but does not substantially change the optical property of the gel.

The effect of salts was explained by the function of anions as ligands; they reacted with titanium hydroxide in a nucleophilic substitution reaction (Eq. 3) to form a hexacoordinated titanium complex (Fig. 6 in the supplementary data) [42]. This complexation alters the directions of germination, ensuring the refraction and passage of light within the material. This result was consistent with findings reported by Hasegawa et al. [40]. Researchers have hypothesized that chloride anions participate in the complexation of Ti^{4+} or act as a Lewis base catalyst for solgel condensation. Here, the partially condensed hydrolysates and Ti atoms became more reactive to nucleophilic attack than the sites. Fewer Ti atoms were hydrolyzed and condensed because the first atom was more deficient in electrons than the latter [43]. Then, the reaction occurs locally and heterogeneously. The hydrolyzed and condensed species react to a greater extent, while unreacted species remain. The difference in transparency between Al^{3+}-, Fe^{3+}- and Sr^{2+}-doped samples was explained by the difference in the electronic forces between Cl^- and NO_3^-, as chloride anions possess a greater nucleophilic component than nitrates [44].

Equation 3:Reaction between the anion of the strong acid and titanium hydroxide.

3.2. Xerogel characterization

3.2.1. Optical characterization

According to the UV-vis-NIR spectra (Fig. 4), all samples were transparent in the visible-NIR range, while they were opaque in the UV range. These results confirm the transparent appearance observed with the naked eye.

The determination of the optical bandgap is obtained using the Tauc equation (Fig. 5) [45]

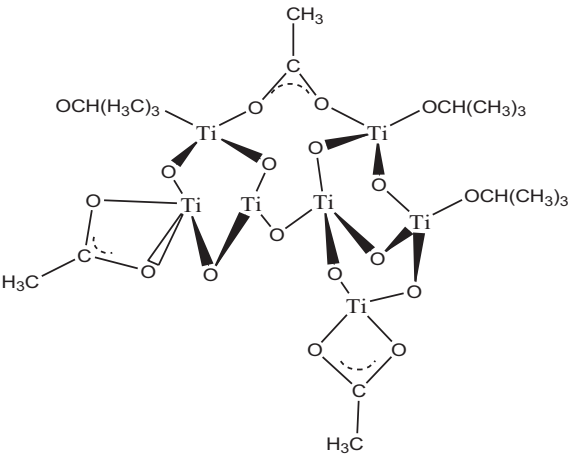

Fig. 2. Germination of gels modified with acetic acid [42].

$$\alpha h\vartheta = A(h\vartheta - E_g)^n \quad (1)$$

where A is a constant, $h\nu$ denotes the photon energy, E_g is the allowed energy gap and $n = 1/2$ for an allowed indirect transition.

The bandgap energy of titanium dioxide doped with aluminium and strontium remains in coincidence with the UV light and is slightly higher than the bandgap energy of pure TiO_2 (Table 2). The increase in the bandgap energy of Al^{3+}-doped TiO_2 is consistent with the results presented by Pathak et al. [46]. Al^{3+} doping creates a nonstoichiometric structure by reducing Ti(IV) to Ti(III). Ti(III) and Al(III) defects induce a shallow energy level below the conduction band that inhibits electron transport and function as electron-trapping sites that cause the slight spreading of the bandgap [47]. On the other hand, the increase in bandgap energy observed for Sr^{2+}-doped TiO_2 contradicts the results reported by Hamedani et al. [48]. This contradiction is potentially explained by the difference in the morphology of synthesized TiO_2.

For Fe^{2+}-doped TiO_2, the bandgap energy was reduced. This reduction results from the presence of Fe(III) species that spread the range of absorbance to the visible region. This shift in absorbance is due to the creation of discrete energetic levels by the electronic transition of the "d" layer of iron, which reduces the forbidden band of the materials [49].

3.2.2. FTIR characterization

The FTIR spectra recorded for the xerogels obtained after drying at 80 °C for 12 h (Fig. 6a) and calcinated at 450 °C for 4 h (Fig. 6b) show the disappearance of many bands after calcination. The bands at a frequency of 661 and 837 cm^{-1} confirm the hydrolysis of the alkoxide and the formation of Ti–O–Ti and Ti–O bonds [36,37,41,50,51]. The two bands at 1028 and 1143 cm^{-1} are assigned to Ti–O–C groups [41,51]. The vibrations of the $-CH_3$ groups of the acetates, the solvent and the isopropanol released by the titanium(IV) tetraisopropoxide adsorbed on the surface of the titanium dioxide are responsible for the appearance of the band at approximately 1350 cm^{-1} [36,41]. The two intense bands observed at 1442 and 1535 cm^{-1} correspond to the symmetrical and asymmetrical vibrations of the carboxyl group (COO), respectively, and result from the formation of a double bond between acetic acid and titanium [51,52]. The band at approximately 3400 cm^{-1} corresponds to the vibration of the lattice bond (O–H), unreacted acetic acid and unreacted solvent [17,52]. The calcined TiO_2 spectra show the persistence of only three bands: a wide band between 500 and 800 cm^{-1} that corresponds to the vibration of the Ti–O–Ti and Ti–O bonds [51,52], a band at a frequency of 1626 cm^{-1} attributed to the vibration of the hydrogen bonds –OH ... O– [17,36,51] and the vibrations of the O–H bonds of the water adsorbed on the surface of the material. The last band located at a frequency of 3400 cm^{-1} is attributed to the terminal O–H group of the crystalline chain, and it is less important than in xerogels dried at 100 °C.

3.2.3. Structural characterization

The X-ray diffractograms of the prepared samples (Fig. 7a) show that the Sr–TiO_2 sample was amorphous, but Fe–TiO_2 and Al–TiO_2 samples displayed peaks at $2\theta = 26°$, $2\theta = 38°$, $2\theta = 48°$ and $2\theta = 54°$, which correspond to the reticular planes (101), (004), (200) and (105) characteristic

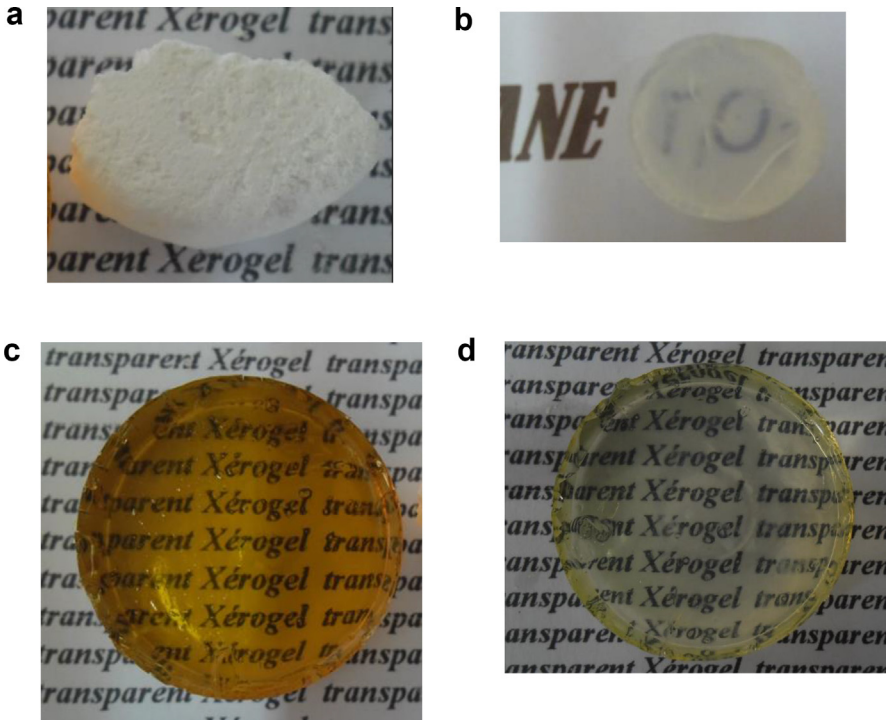

Fig. 3. (a) Nondoped TiO_2 monolith xerogel. (b) Sr–TiO_2 monolith xerogel. (c) Fe–TiO_2 monolith xerogel. (d) Al–TiO_2 monolith xerogel.

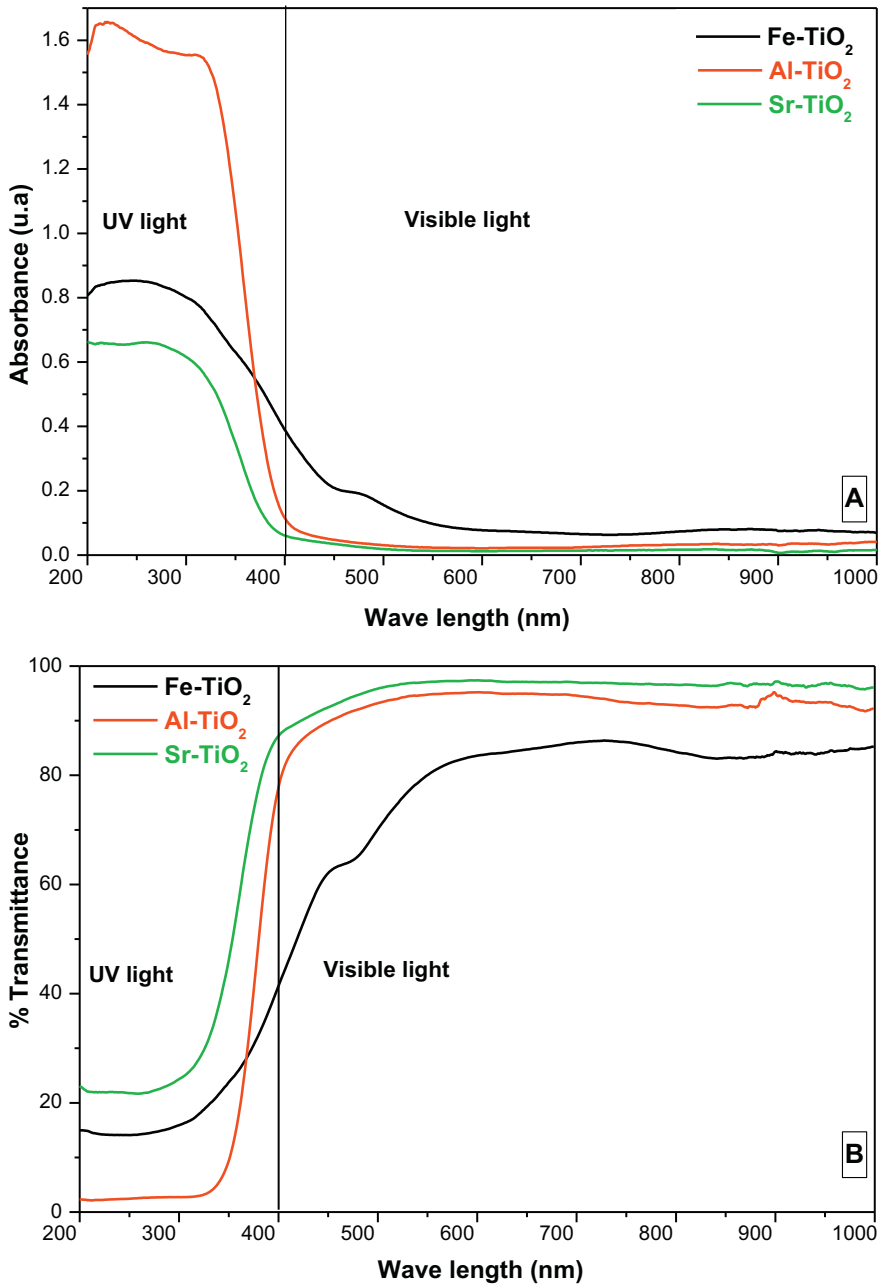

Fig. 4. UV-vis spectra showing the absorbance (a) and % transmittance (b).

of the anatase (PDF 21–1272; space group $I4_1/amd$) phase, respectively [53]. This crystallinity of the as-prepared samples results from the strong acidity of the medium generated by the coexistence of acetic acid and $FeCl_3$ and $AlCl_3$, as the latter are Lewis acids [54,55].

After thermal treatment for 2 h at 450 °C, the diffraction patterns (Fig. 7b) only presented characteristic peaks of the anatase phase of TiO_2 at $2\theta = 26°$, 38°, 48° and 54°, which corresponded to the (101), (004), (200) and (105) planes, respectively, and the intensities of characteristic peaks of anatase were increased in the Fe–TiO_2 and Al–TiO_2 samples. The X-ray diffraction (XRD) spectra of doped titanium dioxide heated at 650 °C (Fig. 7c) displayed the diffraction peaks of the anatase and rutile phases, where 2θ values of 27.58°, 36.30° and 54.42° were attributed to the (110), (101) and (211) planes of the rutile phase (PDF 21–1276; space group $P4_2/mnm$), respectively. In Sr-doped TiO_2, the characteristic peak of brookite phase was detected at $2\theta = 31.8°$, corresponding to the (121) lattice plane [56].

3.2.4. Thermal characterization

In Fig. 3.a and 3.b (in the supplementary data), Al–TiO_2 and Fe–TiO_2 TGA-DTG thermograms showed three stages of weight loss. The first occurred from 30 to 100 °C (weight

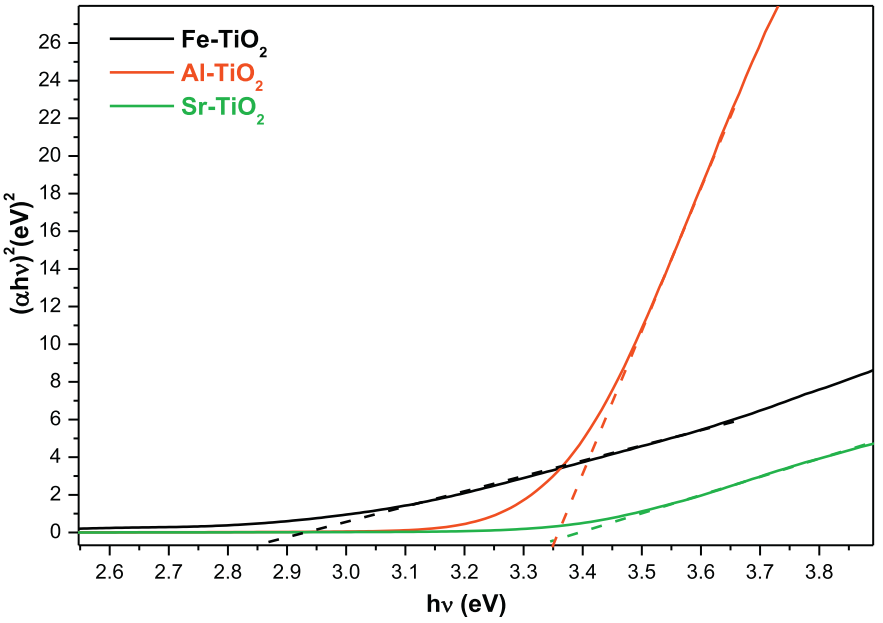

Fig. 5. Tauc plot of $(\alpha h\nu)^2$ versus $(h\nu)$.

Table 2
Gap energy of M-doped TiO_2.

Sample	Experimental gap (eV)	Reference gaps
Fe–TiO_2	2.85	2.50 [49]
Al–TiO_2	3.35	3.12 [47]
Sr–TiO_2	3.34	5.2 [48]
P25	3.25	3.2

loss of 13% for Al–TiO_2 and 10% for Fe–TiO_2), accompanied by an endothermic peak at 100 °C in DTG. This result was probably due to the removal of water and entrapped solvent in the pores of the materials. The second stage was observed between 210 and 440 °C for Al–TiO_2 and approximately between 170 and 270 °C for Fe–TiO_2. These weight losses (weight loss of 9% for Al–TiO_2 and 6% for Fe–TiO_2) were accompanied by an exothermic peak. These weight losses were attributed to the destruction of unbound organic matter (alcohol and acetate). The last weight loss stage occurred from 330 to 440 °C for Al–TiO_2 and from 270 to 400 °C for Fe–TiO_2. The presence of exothermic peak at approximately 400 °C suggest that the weight losses (5.63% for Al–TiO_2 and 4% for Fe–TiO_2) are associated with the decomposition of chelating and banding acetate groups. The phase transition observed in XRD patterns at up to 500 °C was not detected in DTG curves. We deduced that the energy of the transition from the anatase phase to the rutile phase was undetectable with our instrument. The TGA curve of Sr–TiO_2 (Fig. 3.c in supplementary data) shows three weight loss phases. The first occurred between 30 and 150 °C with an endothermic peak in DTG curve. This loss was probably due to the removal of water and entrapped solvent in the pores of the material. The second occurred between 150 and 350 °C and was accompanied by an exothermic peak, due to the decomposition of unbound organic matter. The third weight loss phase was also accompanied by an exothermic peak that is potentially explained by the destruction of bound acetate groups. At 530 °C, another exothermic peak was observed and may result from the appearance of brookite phase detected in XRD analyses.

3.2.5. Textural characterization

The N_2 adsorption/desorption isotherms obtained for the Sr–TiO_2 and Al–TiO_2 samples (presented in supplementary data Fig. 4) are classified as type I. The medium contains only saturated micropores for low values of p/p°. However, no adsorption occurs at higher values that would fill mesopores.

The N_2 adsorption/desorption isotherms of P25 and Fe–TiO_2 are classified as type IV with a very important loop of hysteresis that corresponds to the capillary condensation of the liquid nitrogen in the mesopores. H_2 hysteresis was observed between the adsorption and desorption curves. These hysteresis loops indicate a nonuniform distribution of pore sizes and shapes in our solids. This lack of uniformity may be due to the blockade of pores by the formation of aggregates or bonds between particles [57]. Based on the N_2 adsorption/desorption results, the surface increased with the addition of metallic salts (Table 3). The increase in S_{BET} potentially resulted from the decrease in the nanoparticle size and pore volume.

3.3. Photocatalysis activity

The commercial material Degussa P25–TiO_2 was used as a reference to evaluate the performance of prepared photocatalysts. The performance of the photocatalysts was evaluated upon UV and solar irradiation Fig. 8. After UV irradiation, the photodegradation rates were 76% for

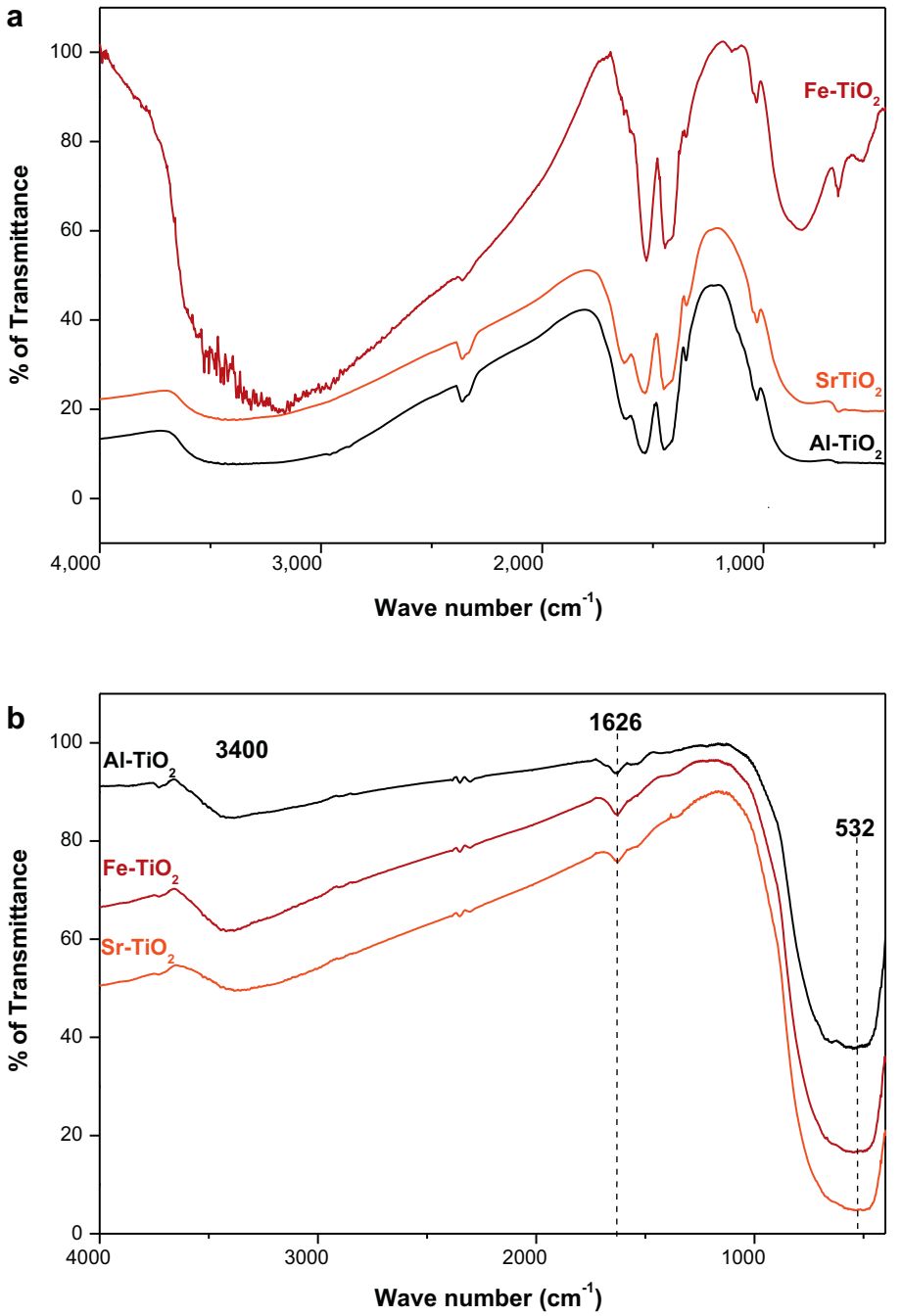

Fig. 6. (a) FTIR spectra of xerogels dried at 80 °C for 12 h. (b) FTIR spectra of xerogels calcinated at 450 °C for 4 h. FTIR, Fourier-transform infrared.

$P25–TiO_2$, 70% for $Al–TiO_2$, 64% for $Sr–TiO_2$ and 54% for $Fe–TiO_2$. The representation of Ln (C_0/C) as a function of time (presented in supplementary data Fig. 5) produced affine lines. The correlation coefficient was very close to 1. Thus, the kinetics of the photocatalytic degradation of MB followed the pseudo-first order. The apparent constants K_{app} of P25, $Al–TiO_2$, $Sr–TiO_2$ and $Fe–TiO_2$ were $0.74 \cdot 10^{-2}$, $0.61 \cdot 10^{-2}$, $0.64 \cdot 10^{-2}$ and $0.36 \cdot 10^{-2}$ min^{-1} with R^2 = 0.9893, 0.9812, 0.9771, and 0.9725, respectively (Table 4). The catalytic activity during the degradation of MB decreased in the following order: P25 > $Al–TiO_2$ > $Sr–TiO_2$ > $Fe–TiO_2$. The transparent $Al–TiO_2$ xerogel exhibited a rate of MB degradation similar to $P25–TiO_2$. The higher photocatalytic efficiency of $Al–TiO_2$ was attributed to the wide bandgap energy and the highest surface area. For Sr-doped TiO_2, the decomposition of BM upon UV irradiation was less effective than P25. However, the degradation rate was still efficient. This difference was attributed to the

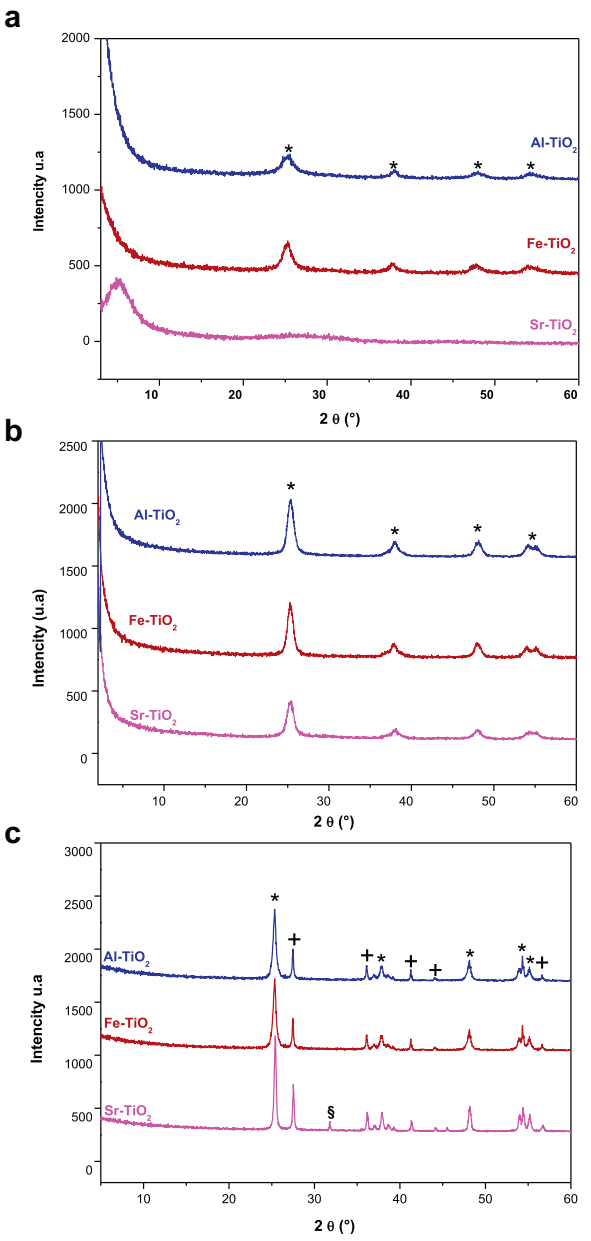

Fig. 7. (a) X-ray diffractograms of noncalcined xerogels; (*) characteristic peaks of the anatase phase. (b) X-ray diffractograms of xerogels annealed at 450 °C; (*) characteristic peaks of the anatase phase. (c) X-ray diffractograms of xerogels annealed at 650 °C; (*) characteristic peaks of the anatase, (+) rutile and (§) brookite phases.

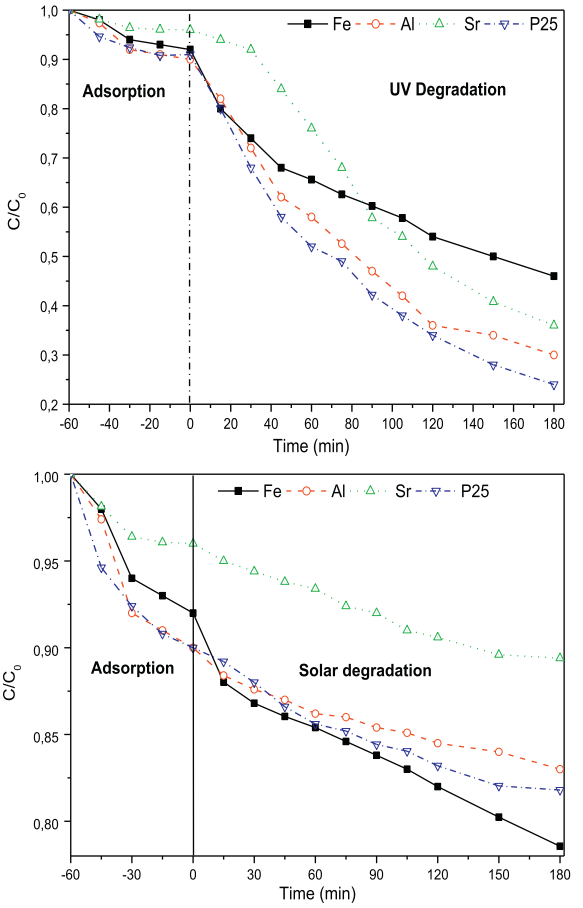

Fig. 8. Variations in (C_0/C) as a function of irradiation time.

Table 4
Kinetics of photodegradation reactions.

Catalyst	UV irradiation		Solar irradiation	
	$K_{app} \times 10^{-2}$ (min^{-1})	R^2	$K_{app} \times 10^{-3}$ (min^{-1})	R^2
P25	0.74	0.9893	0.48	0.9975
Al–TiO_2	0.61	0.9812	0.64	0.9509
Sr–TiO_2	0.64	0.9771	0.42	0.9544
Fe–TiO_2	0.36	0.9725	0.7	0.9751

inhibition of electron-hole recombination owing to the presence of Sr in the TiO_2 lattice [58] and the large surface area of the catalyst. On the other hand, the doping of TiO_2 by Sr ions did not decrease the catalytic activity, mainly because Sr functions as an electron trap and suppresses

Table 3
N_2 adsorption/desorption results for the samples.

Sample	S_{BET} ($m^2 \cdot g^{-1}$)	$S_{Langmuir}$ ($m^2 \cdot g^{-1}$)	S_{Pores} ($m^2 . g^{-1}$)	V_{Pores} ($cm^3 \cdot g^{-1}$)	D_{Pores} (nm)	Nanoparticle size (nm)
Al–TiO_2	304.70	482.24	35.94	0.022	2.46	19.69
Sr–TiO_2	238.82	372.26	11.00	0.006	2.28	25.12
Fe–TiO_2	200.96	345.39	142.04	0.109	3.07	29.85
P25	54.62	123.26	43.71	0.181	2.82	35.32

electron and hole recombination [17,58,59]. Fe-doped TiO_2 was the weakest catalyst upon UV irradiation. A potential explanation for this finding is the low bandgap energy that coincides with visible light and not UV.

After solar irradiation, an analysis of the variation in MB concentration as function of irradiation time in the presence of different catalysts revealed that Fe-doped TiO_2 was the most efficient catalyst, with a yield of degradation $D\% =$ 21.44% after 180 min. This result is consistent with the findings reported by L.L. Costa and A.G.S. Prado [59]. The redshift of the optical absorption spectrum of Fe-doped TiO_2 showed a higher photoabsorption capacity than pure TiO_2, which improved the photocatalytic activity. Fe^{3+} in the network functions as an electron-acceptor (Fe^{3+} Fe^{2+}) and/or hole (Fe^{3+} Fe^{4+}) facilitating the localization of the charge carriers and thus delaying the recombination of the carriers of the charge by trapping them at the dopant level, which forms energy levels close to the conduction or valence bands [60]. Therefore, Fe^{3+} doping of TiO_2 might effectively retard the electron-hole recombination and increase the lifetime, thus improving the photocatalytic activity under solar irradiation. The pseudo-first-order fit of all degradation tests shown in Fig. 5 in supplementary data produced a correlation coefficient close to one in Table 4. Therefore, the kinetics of MB degradation under solar irradiation follow a pseudo-first-order reaction.

4. Conclusions

Based on the findings of the present study, TiO_2-based xerogels are simply synthesized through a succession of hydrolysis and polycondensation reactions of titanium(IV) isopropoxide using the solgel process. Acetic acid was used as the catalyst to generate water through its esterification reaction with the solvent. The most transparent samples are obtained using ethanol as the solvent. According to the DRS analysis, samples are transparent in the visible region. A shift in the bandgap energy towards the visible region for Fe–TiO_2 confirms the incorporation of iron into the anatase structure and reveals the potential of these solids to serve as photocatalysts upon solar irradiation. The bandgap energy decreases as a function of dopant (Fe < Sr < Al). XRD patterns only show the anatase structure for noncalcinated materials and for xerogels calcinated at 450 °C. For xerogels calcinated at 650 °C, characteristic peaks of rutile are present in all samples. The synthesized monoliths are mesoporous and have high surface areas. Upon UV irradiation, Al–TiO_2 degrades 70% of MB after 180 min. This degradation rate is similar to P25. Fe–TiO_2 exhibits greater performance in the solar degradation of MB, with a decomposition yield of 21.44% after 180 min. Theoretical fitting shows that kinetics of the studied decomposition of MB follows a pseudo-first-order model.

Acknowledgements

This study was financially supported by the Tunisian Ministry of Higher Education and Scientific Research and was performed in the Laboratory of Materials, Energy and Environment UR 14/ES 26, University of Gafsa, 2100, Gafsa, Tunisia. The RX analysis was performed at the research centre of the Phosphate Company of Gafsa.

Appendix A. Supplementary data

Supplementary data to this article can be found online at https://doi.org/10.1016/j.crci.2019.10.003.

References

[1] I. Dobrosz-Gomez, M.A. Gomez-Garcia, J. Bojarska, M. Kozanecki, J.M. Rynkowski, C. R. Chimie 18 (2015) 1094–1105.
[2] P.C. Angelomé, L. Andrini, M. Cecilia Fuertes, G. Félix, Requejo, J.A.A. Galo, C.R. Soler-Illia, C. R. Chimie 13 (2010) 256–269.
[3] J. Phalippou, C. R. Chimie 5 (2002) 855–863.
[4] A. Venkateswara Rao, G.M. Pajonk, N.N. Parvathy, E. Elaloui, Sol-Gel Processing and Applications, Plenum Press, New York, 1994, pp. 237–238.
[5] E. Elaloui, P. Achard, B. Chevalier, J.-L. Chevalier, M. Durant, G.M. Pajonk, SPIE 1727 (1992) 402–412.
[6] A. Borne, B. Chevalier, J.L. Chevalier, D. Quenard, E. Elaloui, J. Lambard. J. Non-Cryst. Sol. 210 (1997) 224–231.
[7] H. Hirashima, in: M.A. Aegerter (Ed.), Aerogels Handbook, Springer, New York, Dordrecht, Heidelberg, London, 2011.
[8] N. Husing, U. Schubert, Angew. Chem. Int. Ed. 37 (1998) 23–45.
[9] N. Smirnova, I. Petrik, V. Vorobets, G. Kolbasov, A. Eremenko, Nanoscale Res Lett 12 (2017) 239.
[10] Y. Wang, T. Wu, Y. Zhou, C. Meng, W. Zhu, L. Liu, Sensors 17 (2017) 1971.
[11] Zakrzewska, Radecka, Nanoscale Res. Lett. 12 (2017) 89.
[12] N. Abdullah, S.K. Kamarudin, L.K. Shyuan, N.A. Karim, Nanoscale Res. Lett. 12 (2017) 613.
[13] O.V. Tsymbalyuk, A.M. Naumenko, O.O. Rohovtsov, M.A. Skoryk, I.S. Voiteshenko, V.A. Skryshevsky, T.L. Davydovska, Nanoscale Res. Lett. 12 (2017) 129.
[14] R. Trejo-Tzab, L. Caballero-Espada, P. Quintana, A. Ávila-Ortega, R.A. Medina-Esquivel, Nanoscale Res. Lett. 12 (2017) 32.
[15] R.S. Sabry, Y.K. Al-Haidarie, M.A. Kudhier, J. Sol. Gel Sci. Technol. (2016) 2.
[16] N. Sofyan, A. Ridhova, A.H. Yuwono, A. Udhiarto, IOP Conf. Ser. Mater. Sci. Eng. 316 (2018).
[17] S. Kachbouri, E. Elaloui, Y. Moussaoui, Moroc. J. Chem. (2017) 485–492.
[18] R.M. Mohamed, I.A. Mkhalid, J. Alloy. Comp. (2010) 143–147.
[19] D. Dahlana, S. Khatijah Md Saadb, A. Usra Berlia, A. Bajilia, A. Ali Umar, Physica E (2017) 185–189.
[20] L. Kumar Gaur, P. Kumar, D. Kushavah, K. Roluahpuia Khiangte, M. Chandra Mathpal, V. Agrahari, S.P. Gairola, M.A.G. Soler, H.C. Swart, A. Agarwal, J. Alloy. Compd. 780 (2019) 25–34.
[21] A. Barmeh, M. Reza Nilforoushan, S. Otroj, Thin Solid Films 666 (2018) 137–142.
[22] G. liu, P. Yang, Superlattice Microstruct. 129 (2019) 130–138.
[23] J. Wang, G. Yang, L. Wang, S. Wang, W. Yan, S. Ding, J. Alloy. Compd. 787 (2019) 1110–1119.
[24] Z. Zongyan, Z. Xiang, Y. Juan, L. Qingju, Rare Metal Mater. Eng. 44 (7) (2015) 1568–1574.
[25] K.-R. Kim, S.-H. Lee, S.-W. Paek, H. Chung, J.-H. Yoo, Korean. Chem. Eng. 16 (1) (1999) 34–39.
[26] J.-H. Cho, S.-K. Kim, Sun-Jong Ha, Y.-O. Park, Korean. Chem. Eng. 18 (4) (2001) 456–462.
[27] Joo-Hong, ChoiSung-Kyoung, K.Y.-C. Bak, Korean. Chem. Eng 18 (5) (2001) 719–724.
[28] C. Lu, Y. Chen, L. Tang, S. Wei, Y. Song, J. Wang, Russ. J. Phys. Chem. 91 (7) (2017) 1345–1357.
[29] S. Ni, F. Guo, D. Wang, S. Jiao, J. Wang, Y. Zhang, B. Wang, P. Feng, L. Zhao, Crystals 9 (2019) 113.
[30] S.A. Lermontov, E.A. Straumal, A.A. Mazilkin, A.E. Baranchikov, B.B. Straumal, V.K. Ivanov, Mater. Lett. 215 (2018) 19–22.
[31] B. Yao, L. Zhang, J. Mater. Sci. 34 (24) (1999) 5983–5987.
[32] F. J. Heiligtag, PhD Thesis, ETH Zurich: Zurich, 2014.
[33] N. Kranzlin, F.J. Heiligtag, M. Niederberger, Chimia 68 (2014), 87-87.
[34] F.J. Heiligtag, M.J.I.A. Leccardi, D. Erdem, M.J. Süess, M. Niederberger, Nanoscale 6 (2014) 13213–13221.
[35] G. Hasegawa, K. Kanamori, K. Nakanishi, T. Hanada, J. Sol. Gel Sci. Technol. 53 (2010) 59–66.

[36] K. Elghniji, Z. Anna-Rabah, E. Elaloui, Mater. Sci.-Poland 34 (3) (2016) 633–640.
[37] L. El Mir, A. Amlouk, E. Elaloui, M. Saadoun, A.C. Pierre, Mater. Sci. Eng. B 146 (2008) 69–73.
[38] R. Wang, K. Hashimoto, A. Fujishima, M. Chikuni, E. Kojima, A. Kitamura, M. Shimohigoshi, T. Watanabe, Nature 388 (1997) 431–432.
[39] Ö. Kesmez, E. Burunkaya, H. Nadir Kiraz, E. Çamurlu, M. Asiltürk, E. Arpaç, J. Non-Cryst. Solids 357 (2011) 3130–3135.
[40] G. Hasegawa, K. Kanamori, K. Nakanishi, T. Hanada, J. Sol. Gel Sci. Technol. 53 (1) (2010) 59–66.
[41] J. Krishna Murthy, U. Gross, S. Ru1diger, V. Venkat Rao, V. Vijaya Kumar, A. Wander, C.L. Bailey, N.M. Harrison, E. Kemnitz, J. Phys. Chem. B 110 (No. 16) (2006).
[42] R. Parra, M.S. Góes, M.S. Castro, E. Longo, P.R. Bueno, J.A. Varela, Chem. Master. 25 (2008) 1519–1529.
[43] A. Caumont-Potdevin, Matériaux, Université Blaise-Pascal – Clermont-Ferrand-2, France, 2007.
[44] Z. Kebede, N. Retta, Transition Met. Chem. 15 (1990) 417–419.
[45] U. Ibrahim, Gaya, Springer, Dordrecht, The Netherlands, 2014, pp. 17–19.
[46] S.K. Pathak, A. Abate, P. Ruckdeschel, B. Roose, K.C. Gödel, Y. Vaynzof, A. Santhal, S.-I. Watanabe, D.J. Hollman, N. Noel, Alessandro Sepe, U. Wiesner, R. Friend, H.J. Snaith, U. Steiner, Adv. Funct. Mater. 24 (2014) 6046–6055.
[47] A.I. Rafieh, P. kanayake, A. Wakamiy, H. Nakajima, C.M. Lim, Sol. Energy 177 (2019) 374–381.
[48] H.A. Hamedani, N.K. Allam, H. Garmestani, M.A. El-Sayed, J. Phys. Chem. C 115 (2011) 13480–13486.
[49] T. Barkhade, I. Banerjee, Mater. Today: Proc. 18 (2019) 1204–1209.
[50] Y. Cong, J. Zhang, F. Chen, M. Anpo, D. He, J. Phys. Chem. C 111 (2007) 10618.
[51] C. Ouled Amor, K. Elghniji, C. Virlan, A. Pui, E. Elaloui, Physica B: Phys. Condens. Matter (2019), https://doi.org/10.1016/j.physb.2019.02.017.
[52] J. Ah Chang, M. Vithal, I. Chan Baek, S. Il Seok, J. Solid State Chem. 182 (2009) 749–756.
[53] H. Zhang, J.F. Banfield, J. Phys. Chem. B 104 (2000) 3481–3487.
[54] N. Juha-Pekka, N. Kanerva, T. Mantyla, J. Cryst. Growth 304 (2007) 179–183.
[55] H. Cheng, J. Ma, Z. Zhao, L. Qi, Chem. Mater. 7 (1995) 663–671.
[56] X. Lu, Y. Ma, B. Tian, J. Zhang, Solid State Sci. 12 (2010) 036.
[57] J. Lynch (dir.), Analyse physico-chimique des catalyseurs industriels. Manuel pratique de caractérisation, Technip, Paris, 2001, 08-09.
[58] S. Sood, et al., Ceram. Int. 41 (2015) 3533–3540.
[59] L.L. Costa, A.G.S. Prado, J. Photochem. Photobiol. A Chem. 201 (2009) 45–49.
[60] S. Mansingh, D.K. Padhi, K.M. Parida, Int. J. Hydrogen Energy 41 (2016) 14133–14146.